Single-Particle Light Scattering: Imaging and Dynamical Fluctuations in the Polarization and Spectral Response

Haw Yang[†]

Department of Chemistry, University of California at Berkeley and Physical Biosciences Division, Lawrence Berkeley National Laboratory, Berkeley, California 94720

Received: February 9, 2007; In Final Form: March 16, 2007

A theoretical framework for light scattering from individual nanoscale particles or structures is developed. The main considerations distinguishing the present treatment from the theories developed for conventional light-scattering experiments are the experimental requirements for the detection of the limited light from a single scatterer. These requirements include use of a high numerical aperture microscope objective, annular illumination, and the reduced linear dichroism instead of depolarization ratio. It is shown how these issues are considered in relating the microscopic polarizability tensor to the far-field experimental observables. The approach is further extended to include the dynamical response in the scattering polarization and spectrum and discussed in the context of the particle's rotational diffusion. For dynamic light scattering, analytical expressions are derived to elucidate the interrelationship between the experimental configuration, the observable, the polarizability tensor, and the diffusion tensor. Specific examples including static imaging and dynamic correlation for rodlike and spheroidal scatterers are discussed to illustrate the application of the theory.

1. Introduction

The use of light scattering to investigate individually isolated particles and structures is a relatively new development that provides a direct means to image and probe nanoscale objects well beyond the diffraction-limited optical resolution.[1] It is particularly advantageous for far-field studies of nanostructures that do not luminesce intensely. Recent examples include carbon nanotubes,[2,3] iron oxides,[4] gold nanoparticles[5−8] and nanorods,[9] silver nanoparticles,[10,11] nanocubes,[9] and nanoprisms,[12,13] to name a few (for brevity, particle and nanoparticle are used interchangeably hereafter to represent nanoscale objects that are amenable to such light scattering studies). Because the particles are investigated one at a time, the distribution of a certain particle property in a population can also be studied in detail.[14] This is especially important for the basic research of nanoscale structures, which usually exhibit a variety of shapes and sizes in a sample due to difficulties in the precise control of these parameters. Further, because the spectroscopic characteristics of the scattered light also depend on the dielectric response of the scatterer's medium,[15,16] single-particle light scattering in principle can be used to probe changes in its local environment. Although most of the studies to date have focused on the frequency component of the scattering light, the inclusion of other spectroscopic observables such as polarization should be valuable in providing such additional information as rotational motion[17] as well as the shape of the scatterer.[8,18] The goal of this work is to outline a theoretical framework allowing one to quantitatively relate experimental observations both to the static orientation and to the dynamical rotation of a single scatterer.

The treatment of single-particle light scattering differs from the more extensively studied bulk dynamic light scattering measurements[19] in the way in which experimental observables are defined and averaged. In conventional dynamic light scattering, heterodyne-detected depolarization correlation functions are used to extract rotational dynamics whereas in single-particle light scattering, the reduced linear dichroism is typically used to extract rotational dynamics. Further, to relate the heterodyne-detected interferometric correlation to intensity depolarization correlation in bulk dynamic light scattering, it is necessary to assume that the scattered light originates from a large number of independent light scatterers.[19] This assumption breaks down in single-particle dynamic light scattering where there is only one light scatterer. The second distinct feature of single-particle light scattering has to do with the way experiments are conducted. Due to the small scattering cross section of a single nanoparticle, a microscope objective of high numerical aperture is typically used to collect the scattered light. Under this configuration, the large solid angle of collection has to be included in the analysis for both static imaging and dynamic correlations. Indeed, for fluorescence single-molecule experiments, it has been shown that it is important to specifically include the effect of light-collecting lens in imaging the dipole emission pattern[20,21] and the dipole orientation.[22] It has also been shown that the time correlation of reduced linear dichroism is non-exponential.[23,24] It is therefore expected that issues of this nature should also play an important role in the interpretation of single-particle scattering experiments and need to be clarified. On the other hand, with the rapid advancement of new experimental schemes, quantitative analyses of experimental results are anticipated to help make new observations.

This paper presents for the scattering problem a consistent theoretical framework that includes the aforementioned considerations in both the static and the dynamic cases. The discussion focuses on the polarization and spectral response of the scattered light, as well as on their time dependence in the context of rotational diffusion. The derivation is restricted to classical linear optics with homogeneous materials in which the experimental signal is recorded using a homodyne-detected square-law detector such as avalanche photodiodes and photomultiplier tubes. The theoretical structure nonetheless should

[†] E-mail: hawyang@berkeley.edu.

10.1021/jp071129z CCC: $37.00
Published on Web 05/18/2007

be extensible to include illumination by a focused laser beam[3,6] or by evanescent fields,[25,26] and also to experiments that detects nanoparticles interferometrically.[27] It is hoped that the current analysis may contribute to the fundamental understanding of nanoscale structures as well as to encourage further development of more advanced spectroscopic schemes.

The outline of the article is as follows: Section II describes the theoretical framework that is suitable for single-particle light scattering experiments. It emphasizes the transformation between the microscopic, polarizability frame, and the laboratory frame because these transformations give rise to the experimental observables. This procedure is general and allows a unified treatment of different experimental schemes that may result in different time-dependent observations. In section III, the case of scattering from an immobilized particle is discussed. Here, it is assumed that the particle moves very slowly such that the experimental time resolution is sufficient to resolve its movements. This way, the particle can be viewed as "static" on the experimental time scale. The results can be directly extended to time-dependent imaging. To illustrate the use of the theory described in section II, the discussion begins with a simple case where a rodlike scatterer (only one appreciable polarizability component) is illuminated at a fixed angle. It then develops to include the case where the rodlike scatterer is illuminated annularly (dark-field illumination). As an application of these results, a method to rapidly image the orientation of individual rodlike scatterer is also presented, providing a theoretical basis for studying the time-dependent orientation changes of a nanoscale scatterer. To illustrate the use of the theory for more complicated cases, this section concludes with the discussion of another frequently encountered case, scattering by a single spheroid with annular illumination. In general, though single-particle or the single-molecule dynamics are most revealing, they are also the most challenging both theoretically and experimentally. Section IV extends the treatment to dynamic light scattering focusing on the treatment of rotational diffusion of the particle. This section is motivated by a recent experimental development that in principle will enable spectroscopic measurements on a nanoprobe freely moving in the three-dimensional space.[14,28]

2. Theoretical Framework for Single-Particle Light Scattering

A. Coordinate Systems and the Transformations between Them. There are three frames of reference involved in the process. They are (1) the body-fixed frame associated with the polarizability tensor of the target particle, (2) the laboratory frame, and (3) the frame associated with the electric field of the incident or scattered radiation. The transformation between these coordinate systems connects experimental observations to the microscopic properties of the particle under study. When appropriate, vectors or transformations associated with these frames are denoted by a subscript P, L, and E, respectively.

The polarizability frame is defined by the principal axes of the electric polarizability tensor for the particle,

$$\alpha_{\mathrm{p}}[\epsilon_m(\omega)] = \begin{pmatrix} \alpha_1(\epsilon_{\mathrm{m}}(\omega)) & 0 & 0 \\ 0 & \alpha_2(\epsilon_{\mathrm{m}}(\omega)) & 0 \\ 0 & 0 & \alpha_3(\epsilon_{\mathrm{m}}(\omega)) \end{pmatrix} \quad (1)$$

corresponding to the $\hat{1}$, $\hat{2}$, and $\hat{3}$ directions (cf. inset in Figure 1), where $\epsilon_{\mathrm{m}}(\omega)$ is the complex permittivity of the particle relative to its medium. The laboratory frame is based on the experimental setup and serves as the primary coordinate of

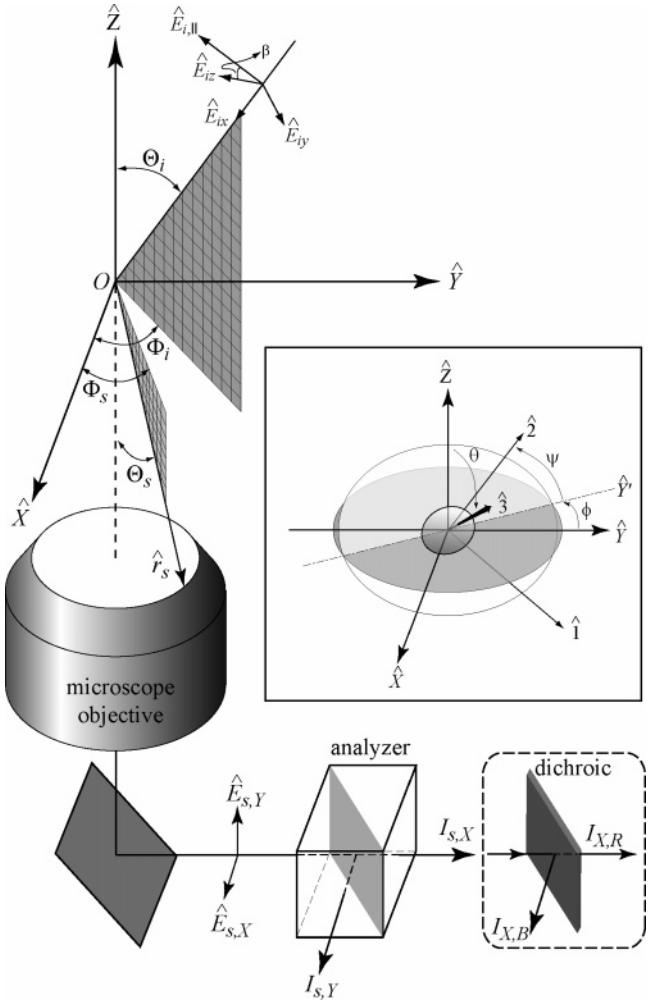

Figure 1. Relative orientation of various reference frames in single-particle scattering experiments. The laboratory frame is defined by the unit vectors $\hat{X}$, $\hat{Y}$, and $\hat{Z}$. The nanoparticle is assumed to reside at the origin, *O*, which is also the focus of the microscope objective lens. The E-field frame is defined by the propagation direction (along $\hat{E}_{i,x}$) and polarization (along $\hat{E}_{i,z}$) of the electric magnetic field, $\vec{E}$ ($\hat{E}_{i,y} = \hat{E}_{i,z} \times \hat{E}_{i,x}$, where $\times$ denotes an outer product). Field components parallel and perpendicular to the $E_{i,x} - \hat{Z}$ incident plane is denoted as $E_{i,||}$ and $\vec{E}_{i,\perp}$, respectively ($\vec{E}_{i,x}$ not shown for clarity). The field polarization assumes an angle β relative to the incident plane. The incident filed impinges on the particle with zenith Θ_i and azimuth Φ_i with respect to the laboratory frame. The scattered field propagates along the $\hat{r}_{\mathrm{s}}$ direction with azimuth Φ_{s} at an angle of Θ_{s} relative to the $-\hat{Z}$ direction. The $\hat{X}$- and $\hat{Y}$-polarized scattered fields after the microscope objective are denoted $\hat{E}_{\mathrm{s},X}$ and $\hat{E}_{\mathrm{s},Y}$, respectively. The inset shows the transformation from the body-fixed polarizability tensor frame (defined by unit vectors $\hat{1}$, $\hat{2}$, and $\hat{3}$) to the laboratory frame through the Euler angles, θ, ψ, and ϕ. The $\hat{Y}'$ vector denotes the intersection of the $\hat{X}-\hat{Y}$ and the $\hat{1}-\hat{2}$ planes. The dashed box at the bottom shows an experimental configuration for the analysis of spectral fluctuations. $I_{X,\mathrm{B}}$ and $I_{X,\mathrm{R}}$ denote respectively the detected intensities for the blue and the red spectral components in the *X*-polarized scattering light.

reference. As shown in Figure 1, with the target particle at the origin *O*, the *Z*-axis is defined as the direction away from the microscope objective; therefore, the scattered field is collected at the $-\hat{Z}$ direction. The *X*- and *Y*-axes are defined by the specific experimental configuration, for example, by the polarization analyzer or by the direction of the incident light.

The E-field frame is defined by the propagation direction and polarization of the electric magnetic field, $\vec{E}$. For the incident field (denoted by subscript i), its propagation direction is considered to be along the $\hat{E}_{\mathrm{i},x}$ direction with its polarization

along the $\hat{E}_{i,z}$ direction ($\hat{E}_{i,y}$ is defined through $\hat{E}_{i,y} = \hat{E}_{i,z} \times \hat{E}_{i,x}$, where $\times$ denotes an outer product),

$$\hat{E}_{i,E} = \hat{E}_{i,z} = \begin{pmatrix} 0 \\ 0 \\ 1 \end{pmatrix} \quad (2)$$

The incident field impinges on the particle with zenith Θ_i and azimuth Φ_i with respect to the laboratory frame. The $\hat{E}_{i,x}$ and the $\hat{Z}$ vectors define the incident plane. Field components parallel and perpendicular to the incident plane are denoted as $\vec{E}_{i,||}$ and $\vec{E}_{i,\perp}$, respectively ($\vec{E}_{i,\perp}$ not shown for clarity).[15] Such a separation of incident polarizations allows a relatively straightforward treatment for polarized and unpolarized illumination. In general, the polarization assumes an angle β relative to the incident plane.

The scattered field (denoted by subscript s) propagates along the $\hat{r}_s$ direction with azimuth Φ_s at an angle of Θ_s relative to the $-\hat{Z}$ direction, expressed in the laboratory-frame coordinate as

$$\hat{r}_s = \cos(\Phi_s)\sin(\pi-\Theta_s)\hat{X} + \sin(\Phi_s)\sin(\pi-\Theta_s)\hat{Y} + \cos(\pi-\Theta_s)\hat{Z} \quad (3)$$

Similar to the incident field, the $\hat{r}_s$ and $\hat{Z}$ vectors define the scattering plane. The scattered field is collected by a collimating lens, usually by a microscope objective of high numerical aperture (NA). After coming out the collimating lens, the scattered field is directed through a polarization analyzer or spectral analyzer, and detected by a square-law detector through $I_{obs} \propto |\vec{E}_{obs}|^2$, where I_{obs} is the detected photon intensity for the polarization or spectral observables.

These different reference frames can be related to each other using the Euler angles. The Euler angles used here follow the $Z-Y-Z$ convention with counterclockwise rotation.[29] These frame transformations are achieved by the following Cartesian rotation matrices,

$$\mathbf{R}_x[\theta] = \begin{pmatrix} 1 & 0 & 0 \\ 0 & \cos\theta & \sin\theta \\ 0 & -\sin\theta & \cos\theta \end{pmatrix}$$

$$\mathbf{R}_y[\theta] = \begin{pmatrix} \cos\theta & 0 & -\sin\theta \\ 0 & 1 & 0 \\ \sin\theta & 0 & \cos\theta \end{pmatrix}$$

$$\mathbf{R}_z[\theta] = \begin{pmatrix} \cos\theta & \sin\theta & 0 \\ -\sin\theta & \cos\theta & 0 \\ 0 & 0 & 1 \end{pmatrix} \quad (4)$$

Therefore, the transformation of a vector $\vec{p}_P$ from the polarizability frame to the laboratory frame is given by

$$\vec{p}_L = \mathbf{R}_{LP}\vec{P}_P \quad (5)$$

where

$$\mathbf{R}_{LP} = (\mathbf{R}_{PL})^{-1} = (\mathbf{R}_z[\psi]\,\mathbf{R}_y[\theta]\,\mathbf{R}_z[\phi])^{-1} \quad (6)$$

For brevity, the Euler angles (ψ, θ, ϕ) are denoted Ω in section IV when discussing the rotational dynamics. The transformation of a vector $\vec{E}_E$ from the E-field frame to the laboratory frame is given by

$$\vec{E}_L = \mathbf{R}_{LE}\vec{E}_E \quad (7)$$

where

$$\mathbf{R}_{LE} = \mathbf{R}_z[\pi-\Phi_i]\,\mathbf{R}_y[-(\pi/2-\Theta_i)]\,\mathbf{R}_x[\beta] \quad (8)$$

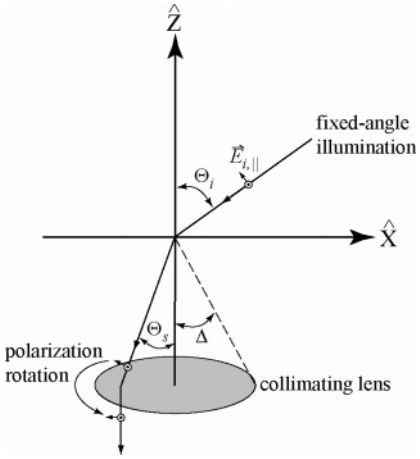

Figure 2. Scheme for a fixed-angle illumination configuration. Note how the polarization of a scattered light is rotated by the collimating lens.

The propagation of the scattered field is redirected by the collimating lens that also changes the direction of the polarization.[20−22] In contrast to the above-discussed coordinate transformations for a vector fixed in space, the collimating lens physically rotates the polarization (cf. Figure 2). The rotation imparted by the collimating lens can be related to the scattering angles Θ_s and Φ_s. Following Axelrod[30] and Fourkas[22] this is accomplished by first rotating the scattering vector $\hat{r}_s$ (cf. eq 3) about the $\hat{Z}$-axis clockwise by Φ_s so that the scattering plane coincide with the $\hat{X}-\hat{Z}$ plane, followed by rotating about the $\hat{Y}$-axis counterclockwise by $\pi - \Theta_s$ (note that when $\Theta_s = 0$, the scattering light propagates along the $+\hat{Z}$ direction), and finally rotating again about the $\hat{Z}$-axis counterclockwise by Φ_s. These rotation operations redirect the scattering field to propagate along the $-\hat{Z}$ direction and correspond to the rotation matrix,

$$\mathbf{R}_{zr} = \mathbf{R}_z[-\Phi_s]\,\mathbf{R}_y[-(\pi-\Theta_s)]\,\mathbf{R}_z[\Phi_s] \quad (9)$$

Finally, only the scattering rays that propagate within the solid angle, $0 \le \Phi_s < 2\pi$ and $\pi - \Delta \le \Theta_s \le \pi$, will be collected by the collimating lens. Here, Δ is related to the numerical aperture of the collimating lens by

$$\Delta = \sin^{-1}(\mathrm{NA}/n_0) \quad (10)$$

where n_0 is the index of refraction of the medium.

B. Experimental Observables. The task at hand is to relate the experimental observables, $I_{s,X}$ and $I_{s,Y}$, to the orientation of the induced dipole $\vec{p}_L$. In general, this dipole approximation is valid when the particle size is much less than a characteristic linear dimension, $\lambda/(2\pi|\epsilon_m - 1|)$. In practice, the theoretical framework should be directly applicable so long as the dipole approximation can be verified experimentally, e.g., via a separate control experiment. With these in mind, one begins by considering a particle that is immobilized at the origin and is illuminated by a monochromatic field at an optical frequency ω. Following Bohren and Huffman,[14] the incident field induces a dipole moment,

$$\vec{p}_L = \epsilon_m \boldsymbol{\alpha}_L \vec{E}_{i,L} \quad (11)$$

$\boldsymbol{\alpha}_L$ is the particle's polarizability tensor in the laboratory frame and can be related to the particle's principal axes of polarizability

by $\alpha_L = \mathbf{R}_{LP}\alpha_P\mathbf{R}_{PL}$. For clarity, the frequency dependence of ϵ_m and α is not explicitly expressed. The scattered radiation at the far field is therefore proportional to $\hat{r}_s \times (\hat{r}_s \times \widehat{p}_L)$.[15]

The scattering field that goes through the collimating lens and reaches the detectors is

$$\vec{E}_{detector} = W_0\mathbf{R}_{zr}\hat{r}_s \times (\hat{r}_s \times \widehat{p}_L) \tag{12}$$

where

$$\widehat{p}_L = \alpha_L\hat{E}_{i,L} = (\mathbf{R}_{LP}\alpha_P\mathbf{R}_{PL})(\mathbf{R}_{LE}\hat{E}_{i,E}) \tag{13}$$

is the dipole moment induced by an incident field with unit amplitude, and $W_0 \propto ik^3E_i/(4\pi\epsilon_m)$ is a constant where the proportionality takes into account such experimental factors as the transmission coefficients in optics and detector efficiency. At this point, $\vec{E}_{detector}$ is a function of the incident light frequency (ω) and its direction (β, Θ_i, Φ_i), the orientation of the particle (θ, ϕ, ψ), the scattering direction (Θ_s, Φ_s), and the numerical aperture of the collimating lens (a function of Δ). The intensities as registered by the square-law detectors after the polarization analyzer are

$$\begin{aligned} I_{s,X\text{ or }Y}(t) &\propto \frac{1}{4\pi}\int_0^{2\pi} d\Phi_s \int_{\pi-\Delta}^{\pi} |\vec{E}_{detector,X\text{ or }Y}(t)|^2 \sin\Theta_s\, d\Theta_s \\ &= I_0\Big(\frac{1}{4\pi}\int_0^{2\pi} d\Phi_s \int_{\pi-\Delta}^{\pi} |\mathbf{R}_{zr}\hat{r}_s \times \\ &\qquad (\hat{r}_s \times \widehat{p}_L(t))_{detector,X\text{ or }Y}|^2 \times \sin\Theta_s\, d\Theta_s\Big) \end{aligned} \tag{14}$$

where the X and Y components can be easily extracted from the Cartesian $\vec{E}_{detector}$ vector in the laboratory frame using $\vec{E}_{detector,X} = (1,0,0)\cdot\vec{E}_{detector}$ and $\vec{E}_{detector,Y} = (0,1,0)\cdot\vec{E}_{detector}$. The intensities I_s and I_0 here can have any unit that represents experimental observables. For example, if the scattering field is detected by a photon-counting detector, the intensity is then defined as number of detected photons per unit time. Clearly, the polarization state of $\vec{E}_{detector}$ is dependent on the incident light, as is expected for scattering experiments. For example, eq 14 is directly applicable to experiments that utilize polarized incident light such as a laser. For an unpolarized illumination light source, such as a lamp, the scattering intensity can be calculated by combining the scattering intensities resulting from $\vec{E}_{i,||}$ and $\vec{E}_{i,\perp}$ illuminations,[15] $I_{s,unpolarized} = I_s(\vec{E}_{i,||}) + I_s(\vec{E}_{i,\perp})$. In single-molecule or single-particle experiments, the polarization state of the emission or scattered light is typically expressed in terms of the reduced linear dichroism, defined as

$$\chi_d \equiv \frac{I_X - I_Y}{I_X + I_Y} \tag{15}$$

Equation 14 signifies an important difference between the observables from the conventional dynamic light scattering experiment and a single-particle scattering experiment. In the latter, there is no ensemble averaging in the experimental observable. Instead, the experimental observable is averaged over time to attain appropriate signal-to-noise ratio. The explicit time parameter in the equation illustrates this point. In practice, the experimental observable is recorded by integrating the intensity over a period of δ, $\bar{I}_s(t)\delta = \int_{t-\delta/2}^{t+\delta/2} I_s(t')\, dt'$. In the following section for static scattering, the explicit dependence in time is omitted for clarity.

3. Light Scattering From an Immobilized Single Particle

To illustrate the application of the theoretical treatment, one may begin with a case in which the target particle exhibits an appreciable polarizability only along the 3 axis. For all practical purposes, such a scatterer may be considered a "rod." The results for this simple case will be compared with results from more complicated scenarios dealing with spheroidal scatterers. The polarization property of the scattering light from a rodlike scatterer is analogous to, and can be compared with, a well-defined emission dipole from a single fluorescent molecule. Experimentally, one may select a certain frequency such that only one of the three principal polarizability components is responsive to the incident light. Examples include the scattering of a single gold nanorod[31] and single carbon nanotubes.[2]

Two experimental configurations will be discussed for the rodlike scatterer. In one configuration, the incident beam impinges on the target particle with a fixed direction with respect to the laboratory frame, typically at an oblique angle with respect to the $\hat{X}-\hat{Y}$ plane.[2,3] In the other configuration, the incident light constitutes an annular cone as in a dark-field microscope. It is assumed the particle is immobilized, such that its surrounding medium can be considered to exhibit a homogeneous electric permittivity. Additional symmetry axes will need to be taken into account if there is a mismatch in the index of refraction in the immediate vicinity of the particle.[32] Nevertheless, the same theoretical framework should be applicable to relating any polarizability tensor to experimental observables.

A. Illumination at a Fixed Incident Direction. Without loss of generality, the incident plane is assumed in this case to coincide with the $\hat{X}-\hat{Z}$ plane ($\Phi_i = 0$, cf. Figure 2). The polarization of the incident light can be either parallel ($\beta = 0$, corresponding to $\vec{E}_{i,||}$) or perpendicular ($\beta = \pi/2$, $\vec{E}_{i,\perp}$) to the plane of incidence. Using eqs 2, 6, 8, and 13, the unit electric field-induced dipole moments expressed in the laboratory frame are

$$\begin{aligned} \widehat{p}_{L,||} &= \alpha_3\begin{pmatrix} \sin\theta\cos\phi(-\cos\phi\sin\theta\cos\Theta_i + \cos\theta\sin\Theta_i) \\ \sin\theta\sin\phi(-\cos\phi\sin\theta\cos\Theta_i + \cos\theta\sin\Theta_i) \\ \cos\theta(-\cos\phi\sin\theta\cos\Theta_i + \cos\theta\sin\Theta_i) \end{pmatrix} \\ \widehat{p}_{L,\perp} &= \alpha_3\begin{pmatrix} -\sin^2\theta\cos\phi\sin\phi \\ \sin^2\theta\sin^2\phi \\ \cos\theta\sin\theta\sin\phi \end{pmatrix} \end{aligned} \tag{16}$$

As expected, $\widehat{p}_{L,\perp}$ does not depend on the incident zenith angle, Θ_i. The magnitudes of these induced dipoles depend on the orientation of the particle relative to the direction and the polarization of the incident light, given by

$$\begin{aligned} |\widehat{p}_{L,||}|^2 &= \alpha_3{}^2(\sin\theta\cos\phi\cos\Theta_i - \cos\theta\sin\Theta_i)^2 \\ |\widehat{p}_{L,\perp}|^2 &= \alpha_3{}^2\sin^2\theta\sin^2\phi \end{aligned} \tag{17}$$

The experimental observables $I_{s,X}$ and $I_{s,Y}$ are calculated using eqs 9, 14, 16, and 17. It turns out that both parallel and perpendicular illumination result in the same expression for the scattering intensity. The X and the Y polarization components are

$$I_{s,||/\perp,X} = I_0|\widehat{p}_{L,||/\perp}|^2(A + B\sin^2\theta + C\cos 2\phi\sin^2\theta) \tag{18}$$

and

$$I_{s,||/\perp,Y} = I_0|\widehat{p}_{L,||/\perp}|^2(A + B\sin^2\theta - C\cos 2\phi\sin^2\theta) \tag{19}$$

respectively. In the above equations, $A = {}^1/_6 - {}^1/_4\cos\Delta + {}^1/_{12}\cos^3\Delta$, $B = {}^1/_8\cos\Delta - {}^1/_8\cos^3\Delta$, and $C = {}^7/_{48} - {}^1/_{16}$

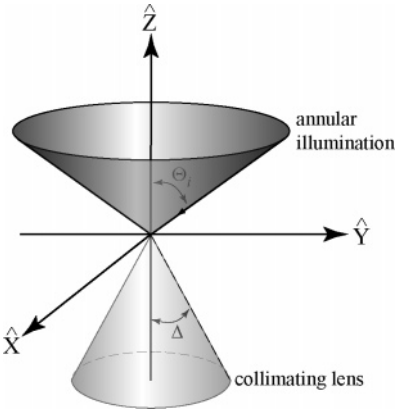

Figure 3. Scheme for an annular illumination configuration.

$\cos\Delta - {}^1/_{16}\cos^2\Delta - {}^1/_{48}\cos^3\Delta$ are coefficients as defined by Fourkas.[22] Because these coefficients only depend on the numerical aperture of the collimating lens (cf. eq 10), they are therefore constants for a given experimental setup.

In the limit of $|\hat{p}_{L,||/\perp}|^2 \rightarrow 1$, eqs 18 and 19 become identical to equations derived for single-molecule fluorescence polarizations under circularly polarized excitation (eqs 4a and 4c of Fourkas,[22] respectively). Therefore, the polarization of this scattering problem can be decomposed into two independent contributions. One is due to the relative orientation of the incident beam and the $\alpha_3\hat{3}$ polarizability of the particle, the $|\hat{p}_{L,||/\perp}|^2$ term, whereas the other is due to the relative orientation of the induced dipole (along $\hat{3}$) and the polarization analyzer, the $(A + B\sin^2\theta \pm C\cos 2\phi \sin^2\theta)$ term. Compared with the analysis of fluorescence from a single chromophore, the former is analogous to the excitation and the latter to the emission. Indeed, for a fluorescent singe molecule, if the absorption and emission dipoles overlap, eqs 18 and 19 will be the appropriate equations to use for linearly polarized excitation.

For cases in which the illumination light is unpolarized, the *X*- and *Y*-polarized scattering intensities are simply

$$I_{s,X} = I_{s,||,X} + I_{s,\perp,X} = I_0(|\hat{p}_{L,||}|^2 + |\hat{p}_{L,\perp}|^2)(A + B\sin^2\theta + C\cos 2\phi \sin^2\theta) \quad (20)$$

and

$$I_{s,Y} = I_{s,||,Y} + I_{s,\perp,Y} = I_0(|\hat{p}_{L,||}|^2 + |\hat{p}_{L,\perp}|^2)(A + B\sin^2\theta - C\cos 2\phi \sin^2\theta) \quad (21)$$

respectively. Thus the basic forms of the experimental observables for both the polarized and unpolarized light source are the same for the case of fixed-angle illumination. One next considers a case in which the illumination light forms an annular cone. This configuration is commonly seen when using a commercially available dark-field microscope.

B. Annular Illumination with Unpolarized Light. The treatments of this problem follow those in the previous case. The experimental observables are first calculated separately for the $\vec{E}_{i,||}$- and $\vec{E}_{i,\perp}$-polarized light, then combined at the end to represent the results for illumination from unpolarized light. Instead of having a fixed azimuthal angle for the incident beam, Φ_i is integrated over 0 to 2π (cf. Figure 3). The magnitudes of the induced dipole moments under annular illumination are

$$|\hat{p}_{L,||\bigcirc}|^2 = \frac{1}{2\pi}\int_0^{2\pi} \hat{p}_{L,||}{}^* \cdot \hat{p}_{L,||}\, d\Phi_i = \frac{\alpha_3{}^2}{8}[3 + \cos 2\theta - \cos 2\Theta_i(1 + 3\cos 2\theta)] \quad (22)$$

and

$$|\hat{p}_{L,\perp\bigcirc}|^2 = \frac{1}{2\pi}\int_0^{2\pi} \hat{p}_{L,\perp}{}^* \cdot \hat{p}_{L,\perp}\, d\Phi_i = \frac{\alpha_3{}^2}{2}\sin^2\theta \quad (23)$$

where the "○" symbol in the subscript denotes annular illumination. Note that, compared with eq 17, the magnitude of the induced dipole moment no longer depend on the azimuthal angle ϕ. The scattering intensity is calculated using

$$I_{s,\bigcirc,X \text{ or } Y}(t) = I_0\left(\frac{1}{8\pi^2}\int_0^{2\pi} d\Phi_i \int_0^{2\pi} d\Phi_s \int_{\pi-\Delta}^{\pi} |\mathbf{R}_{zr}\hat{r}_s \times (\hat{r}_s \times \hat{p}_L(t))_{\text{detector},X \text{ or } Y}|^2 \times \sin\Theta_s\, d\Theta_s\right) \quad (24)$$

After some algebraic manipulations, the *X*- and *Y*-polarized intensities in this annularly illuminated configuration are found to be identical to those derived for fixed-angle illumination in eqs 20 and 21, except the induced dipole moments resulting from an incident field polarization parallel or perpendicular to the incident plane are now replaced by eqs 22 and 23, respectively.

The preceding discussions show that, except for the magnitude of the induced dipole moment due to different illumination geometry, the basic formulation for relating the polarization of the scattering light to the orientation of a rodlike scatterer are the same for fixed-angle and for annular illuminations. This further suggests the feasibility of using single-particle light scattering to extract the absolute orientation of a scatterer with unpolarized, annularly illumination. This idea is explored below.

C. Rapid Imaging of the Absolute Orientation of an Immobilized Rodlike Scatterer. A corollary of the previous discussion is that θ and ϕ, and therefore the absolute orientation of the particle's polarizability along $\hat{3}$, can be quickly determined by scattering experiments using a method analogous to that described by Fourkas for single fluorophores.[22] In essence, θ and ϕ can be determined if the scattering fields polarized along the $\Phi_s = 0$ (coincide with the $\hat{X}$-axis, $I_{s,X}$), $\Phi_s = \pi/4$ (45°), $\Phi_s = \pi/2$ (90°, coincide with the $\hat{Y}$-axis, $I_{s,Y}$), and $\Phi_s = 3\pi/4$ (135°) directions are measured. The electric fields that pass through the polarization analyzer and detected by the detector in these cases are $\vec{E}_{\text{detector},0^\circ} = (1,0,0)\cdot\vec{E}_{\text{detector}}$, $\vec{E}_{\text{detector},45^\circ} = (1/\sqrt{2})(1,1,0)\cdot\vec{E}_{\text{detector}}$, $\vec{E}_{\text{detector},90^\circ} = (0,1,0)\cdot\vec{E}_{\text{detector}}$, and $\vec{E}_{\text{detector},135^\circ} = (1/\sqrt{2})(1,-1,0)\cdot\vec{E}_{\text{detector}}$. The scattering light intensity analyzed at these angles can be calculated as before:

$$I_{s,0^\circ} = I_{s,||\bigcirc,0^\circ} + I_{s,\perp\bigcirc,0^\circ} = I_0(|\hat{p}_{L,||\bigcirc}|^2 + |\hat{p}_{L,\perp\bigcirc}|^2)(A + B\sin^2\theta + C\cos 2\phi \sin^2\theta)$$

$$I_{s,45^\circ} = I_{s,||\bigcirc,45^\circ} + I_{s,\perp\bigcirc,45^\circ} = I_0(|\hat{p}_{L,||\bigcirc}|^2 + |\hat{p}_{L,\perp\bigcirc}|^2)(A + B\sin^2\theta - C\sin 2\phi \sin^2\theta)$$

$$I_{s,90^\circ} = I_{s,||\bigcirc,90^\circ} + I_{s,\perp\bigcirc,90^\circ} = I_0(|\hat{p}_{L,||\bigcirc}|^2 + |\hat{p}_{L,\perp\bigcirc}|^2)(A + B\sin^2\theta - C\cos 2\phi \sin^2\theta)$$

$$I_{s,135^\circ} = I_{s,||\bigcirc,135^\circ} + I_{s,\perp\bigcirc,135^\circ} = I_0(|\hat{p}_{L,||\bigcirc}|^2 + |\hat{p}_{L,\perp\bigcirc}|^2)(A + B\sin^2\theta + C\sin 2\phi \sin^2\theta)$$

The orientation of the scatterer, θ and ϕ, can be calculated using a combination of the above equations. There are several ways of achieving this goal; here, only one example is given,

$$\phi = \frac{1}{2}\tan^{-1}\left(\frac{I_{s,135^\circ} - I_{s,45^\circ}}{I_{s,0^\circ} - I_{s,90^\circ}}\right) \qquad \theta = \sin^{-1}\left(\sqrt{\frac{A\chi_d}{C\cos 2\phi - B\chi_d}}\right) \tag{25}$$

where

$$\chi_d = \frac{I_{s,0^\circ} - I_{s,90^\circ}}{I_{s,0^\circ} + I_{s,90^\circ}} = \frac{C\cos 2\phi \sin^2\theta}{A + B\sin^2\theta} \tag{26}$$

is the reduced linear dichroism (cf. eq 15). Equation 25 allows for a rapid determination of a single rodlike scatterer's absolute orientation. The formulas appear very simple because only one principal polarizability component along a particular direction is involved in this scattering problem. For problems involving more than one scattering tensorial component, such as the spheroid scattering problem discussed in the next section, imaging the absolute orientation is expected to become more complicated and is likely to require numerical solutions.

D. Light Scattering from an Immobilized Spheroidal Nanoparticle with Annular Illumination. Another commonly encountered example is light scattering from individual, nearly spherical nanoparticles. For such a nanoparticle with a diameter much less than the wavelength of the interrogating light—therefore, the surface "roughness" is on a length scale that is even much smaller than the size of the particle—its interaction with an electric field can usually be described by the dipole approximation. Consequently, although a nanoscale scatterer in general may appear irregular and nonspherical under a high-resolution electron microscope, these features are usually not identifiable by far-field optical methods. With this in mind, this section outlines the application of the theoretical framework to symmetric spheroid particles.

The polarizability tensor is assumed to be symmetric; that is, $\alpha_1 = \alpha_2 \neq \alpha_3$ in eq 1. For nearly spherical particles, one may further use the isotropic and anisotropic polarizabilities to describe the scattering intensity:

$$\alpha_{iso} \equiv \frac{1}{3}(\alpha_3 + 2\alpha_1) \qquad \text{and} \qquad \alpha_{aniso} \equiv (\alpha_3 - \alpha_1) \tag{27}$$

For perfectly spherical particles ($\alpha_1 = \alpha_2 = \alpha_3$), one has $\alpha_{aniso} = 0$ and $\alpha_{iso} = \alpha_3$. The other limiting case, a rodlike scatterer ($\alpha_1 = \alpha_2 = 0$), gives $\alpha_{iso} = {}^1/_3\alpha_3$ and $\alpha_{aniso} = 3\alpha_{iso}$. The experimentally measured scattering intensities can be calculated as before (using eq 24), but now the illumination and the scattering parts can no longer be separated like those seen in eqs 18 and 19. After some algebraic manipulations, the *X*- and *Y*-polarized intensities are found to be

$$\begin{aligned} I_{s,\bigcirc,X} = {} & \frac{1}{18}[(7A + 3B - 3AH + BH)\alpha_{aniso}^2 - 6(A + 3B + 3AH + \\ & BH)\alpha_{aniso}\alpha_{iso} + 9(4A + 3B + BH)\alpha_{iso}^2] + \frac{1}{12}[(A + 3AH + \\ & 8BH)\alpha_{aniso}^2 + 6(A + 3B + 3AH + BH)\alpha_{aniso}\alpha_{iso}]\sin^2\theta + \\ & \frac{1}{6}[(9C + 3CH)\alpha_{aniso}\alpha_{iso} - 4CH\alpha_{aniso}^2]\cos 2\phi \sin^2\theta + \\ & \frac{1}{4}(C + 3CH)\alpha_{aniso}^2\cos 2\phi \sin^4\theta + \frac{1}{4}(B + 3BH)\alpha_{aniso}^2\sin^4\theta \end{aligned} \tag{28}$$

and

$$\begin{aligned} I_{s,\bigcirc,Y} = {} & \frac{1}{18}[(7A + 3B - 3AH + BH)\alpha_{aniso}^2 - 6(A + 3B + 3AH + \\ & BH)\alpha_{aniso}\alpha_{iso} + 9(4A + 3B + BH)\alpha_{iso}^2] + \frac{1}{12}[(A + 3AH + \\ & 8BH)\alpha_{aniso}^2 + 6(A + 3B + 3AH + BH)\alpha_{aniso}\alpha_{iso}]\sin^2\theta - \\ & \frac{1}{6}[(9C + 3CH)\alpha_{aniso}\alpha_{iso} - 4CH\alpha_{aniso}^2]\cos 2\phi \sin^2\theta - \\ & \frac{1}{4}(C + 3CH)\alpha_{aniso}^2\cos 2\phi \sin^4\theta + \frac{1}{4}(B + 3BH)\alpha_{aniso}^2\sin^4\theta \end{aligned} \tag{29}$$

respectively, where $H \equiv \cos 2\Theta_i$ is also a constant for a given experimental configuration. Notice the sign change in terms that contain $\cos 2\phi$. For a perfectly spherical scatterer, one has $\lim_{\alpha_{aniso}\to 0}(I_{s,\bigcirc,X} - I_{s,\bigcirc,Y}) = 0$, verifying that the reduced linear dichroism for a perfectly spherical scatterer is zero. On the other hand, it can also be easily verified that the linear dichroism, $\chi_d = (I_{s,\bigcirc,X} - I_{s,\bigcirc,Y})/(I_{s,\bigcirc,X} + I_{s,\bigcirc,Y})$, for a spheroidal scatterer reduce to that of a rodlike scatterer in eq 26. This is also verified.

The analytical expressions presented in this section in principle can also be used for dynamic imaging to follow the polarization changes of individual nanostructures in real time. It ought to be noted, however, that the intensities include measurement uncertainties as well as background scattering. These factors are likely to be dependent on the experimental setup and have to be explicitly included in discussing experimental results. For instance, the noise statistics are expected to be different for different detectors; e.g., the data from single-photon-counting avalanche photodiodes should be treated differently than that from a charge coupled device (CCD) camera. The formulas derived here nevertheless provide a convenient venue to analytically incorporate different noise (and background) characteristics. For example, ideas in many of the advanced statistical methods to quantitatively extract the time-dependent behavior developed for single-molecule[33,34] or single-particle[35] experiments should be directly applicable with no or minor modifications. For faster orientational or structural changes, time correlation function is used to recover the underlying dynamics. The correlation approach has the additional advantage that the uncorrelated background and noise does not contribute to the correlation trace. For both the imaging and the correlation applications, it is important for an experimentalist to ensure that the complicating multiple scattering does not contribute appreciably to the experiment.

4. Rotation-Coupled Fluctuations in Light Scattering

Experimentally, dynamic light scattering from a single particle has been obtained by suspending the particle in a medium.[36] A recent example is the study of a single optically trapped 500 nm silica bead, where the translational Brownian motion and the three-dimensional trapping force can be deduced from the dynamical scattering intensity fluctuations.[37] An alternative approach is to let the nanoparticle to be studied freely moving inside the host medium in three dimensions. One then moves the sample container to counteract the translational Brownian movements such that the particle is always at the focus of a microscope.[14,28] With these possible experimental realizations in mind, the theoretical framework outlined below assumes that the translational degree of freedom can be neglected, either by separation of time scale (e.g., particle in a viscous medium) or by actively canceling the translational motion. Such experiments therefore extract the dynamics related to the rotational degree of freedom and potentially can shed light on the manner in which

internal structural fluctuations are coupled to the diffusion tensor. Because the capability to perform this kind of experiment was only recently made possible,[14,28] theoretical treatments appropriate for relating experimental observations to the microscopic dynamics have not yet been developed. It is therefore the goal of this section to put forth such a framework. The discussion will remain in the context of scattering from a single particle exhibiting cylindrical symmetry both in the polarizability tensor and in its diffusion tensor.

A. Basic Formulation. In such experiments, the dynamics are generally contained in the time correlation function of the reduced linear dichroism,

$$\langle \chi_d(t)\, \chi_d(0)\rangle_T = \frac{1}{T}\int_0^T \chi_d(t+\tau)\, \chi_d(\tau)\, d\tau \tag{30}$$

where T is the length of the single-particle scattering time trajectory. As discussed earlier, χ_d is a function of θ and ϕ, which change as functions of time as the particle rotates in three dimensions. In the preceding discussions, θ and ϕ have been used for the development of the theoretical framework because they deliver a relatively more transparent physical picture, for example, in imaging the orientations of single nanoparticles. In the context of discussing rotational motions, however, it is more convenient to use the Wigner rotation matrix elements ($D^{(l)}_{m,n}[\Omega(t)]$; Ω's are Euler angles introduced earlier) to carry out the various coordinate transformations as well as to describe the dynamical behavior. If T is much greater than any time scale that is relevant to rotational relaxation, then the rotational states as given by Ω will have been sufficiently sampled by the particle. Under these conditions, eq 30 can be approximated as

$$\langle \chi_d(t)\, \chi_d(0)\rangle_T \approx \langle \chi_d(t)\, \chi_d(0)\rangle = \int d\Omega(t) \int d\Omega(0)\, \chi_d[\Omega(t)]\, G[\Omega(t)|\Omega(0)] \times \chi_d[\Omega(0)]\, P[\Omega(0)] \tag{31}$$

where $P[\Omega(0)] = (8\pi^2)^{-1}$ is the equilibrium distribution of the rotational states and $G[\Omega(t)|\Omega(0)]$ is Green's function describing the conditional probability of finding the particle at $\Omega(t)$ at time t given that it is at $\Omega(0)$ at time 0. Thus, the rotational dynamics of the particle is contained in Green's function. Here, the discussion will focus on diffusion-type motions following the Stokes−Einstein−Debye relationship.[38] In accordance with the previous discussion for particles exhibiting a polarizability tensor with cylindrical symmetry, the following discussion will further be restricted to the cases where the tensor for three-dimensional diffusion also exhibits cylindrical symmetry.

It is necessary to introduce an additional reference frame associated with the diffusion tensor (denoted by a subscript D wherever appropriate). The diffusion frame, as defined by the principal components of the diffusion tensor, may not necessarily overlap with the polarizability frame. The transformation between them can also be achieved via the Euler angles as before. It is assumed the relative orientation of the diffusion frame with respect to the polarizability frame is also independent of time. This assumption is easily met when the particle under investigation can be viewed as a rigid rotor within the time scale of investigation.

By Favro,[39] Green's function for symmetric-top rigid rotor is

$$G[\Omega_{LD}(t)|\Omega_{LD}(0)] = \sum_{l,m,n}\left(\frac{2l+1}{8\pi^2}\right) D^{(l)}_{mn}[\Omega_{LD}(t)]\, D^{(l)}_{mn}[\Omega_{LD}(0)]^* \times \exp[-l(l+1)D_\perp t + n^2(D_{||} - D_\perp)t] \tag{32}$$

where $D_\perp$ and $D_{||}$ are diffusion coefficients associated with rotational motions about the axes that are perpendicular and parallel to the symmetry axis of the particle, respectively. Notice that this equation is expressed in terms of the relative orientations between the diffusion and the laboratory frames, Ω_{LD}, whereas the reduced linear dichroism calculated using eqs 28 and 29 are based on the relative orientation between the polarizability frame and the laboratory frame, denoted by Ω_{LP}. Equation 31 can be further reduced following the treatments of Szabo[40] for fluorescence depolarization, and those of Hinze et al.[23] for rotational correlation of reduced linear dichroism from single-molecule fluorescence. Briefly, one makes use of the orthogonal properties of the Wigner rotation matrix elements,[29]

$$\int d\Omega\, D^{(l')}_{m',n'}(\Omega)^*\, D^{(l)}_{m,n}(\Omega) = \frac{8\pi^2}{2l+1}\,\delta_{l,ln'}\delta_{m,m'}\delta_{n,n'} \tag{33}$$

to expand the reduced linear dichroism in terms of the matrix elements and obtains

$$\chi_d(t) = \sum_{l,m} K_{l,m} D^{(l)}_{m,0}[\Omega_{LP}(t)] \tag{34}$$

where $K_{l,m} = [(2l+1)/8\pi^2]\int d\Omega\, D^{(l)}_{m,0}(\Omega)^*\chi_d$. $\Omega_{LP}(t)$ in eq 34 and $\Omega_{LD}(t)$ in eq 32 are related by $\Omega_{LP}(t) = \Omega_{LD}(t) + \Omega_{DP}$, where Ω_{DP} is the relative orientation between the polarizability frame and the diffusion frame and is assumed to be time independent. Using the transformation property of the Wigner matrix elements,

$$D^{(l)}_{m,0}[\Omega_{LP}(t)] = \sum_{\mu} D^{(l)}_{m,\mu}[\Omega_{LD}(t)]\, D^{(l)}_{\mu,0}(\Omega_{DP}) \tag{35}$$

and eqs 32−34, eq 31 becomes

$$\langle \chi_d(t)\, \chi_d(0)\rangle = \sum_l \frac{1}{2l+1}\Big[\sum_{m=-l}^{l} |K_{l,m}|^2\Big]\Big[\sum_{n=-l}^{l} |D^{(l)}_{n,0}(\Omega_{DP})|^2 \times e^{-l(l+1)D_\perp t + n^2(D_{||}-D_\perp)t}\Big] \tag{36}$$

It is clear from eq 36 that, in general, the correlation function will exhibit a multiexponential decay, even for the case of symmetric-top diffusers. In general, one may use numerical methods to assess the relative weights of the different l-component exponential decays for single-particle light-scattering experiments, as has been done for fluorescence single-molecule rotations with[24] and without[23] considering the numerical aperture of the collimating lens. Multiple exponential decays in the correlation function from single-particle dynamic light scattering experiments is in contrast to the cases in conventional heterodyne light scattering experiments,[19] and to those in fluorescence depolarization.[40] In both experimental schemes, the observables transform as $l = 2$ spherical harmonics (or $l = 2$ Wigner rotation matrices) such that only the $l = 2$ components in the rotational diffusion Green's function are selected. Hence, the maximum number of exponentials in the polarization correlation for symmetric-top diffusers is 3. The exact form of the time correlation function such as the number of exponentials critically depends on how the experimental observables are measured and defined. For example, in eq 36 the observable is defined by $\chi_d = (I_X - I_Y)/(I_X + I_Y)$, where the homodyne detected intensities I_X and I_Y are measured. The correlation function is further shaped by the experimental configuration such as the illumination and collimation numerical aperture (contained in the $K_{l,m}$ parameter in eq 36), as well as by the polarizability tensor $\boldsymbol{\alpha}$ (also contained in $K_{l,m}$), the diffusion tensor $\mathbf{D}$ (appearing in the exponent), and

the coupling between them (contained in $D^{(l)}_{n,0}(\Omega_{DP})$). Therefore, these analytical expressions allow one to evaluate different contributions separately affording a quantitative interpretation of the experimental results. For example, a metallic nanoparticle can be considered as a rigid rotor with its polarizability related to its shape by electrostatic approximation (cf. eq 45). This, in turn, allows one to investigate the dynamical interactions between the scatterer (now can be viewed as a nanoprobe) and its microscopic environment, contained in the diffusion coefficients $D_\perp$ and $D_{||}$.[35]

In practice, considering the strongly stochastic nature of single-molecule or single-particle time trajectories and the experimental noise contained within them, the experimental data may not be able support multiexponential models with sufficient statistical confidence. For example, an $l = 2$ decay relaxes with a rate of $\sim 6D_\perp$ whereas an $l = 4$ decay relaxes with a rate that is 3 times greater ($\sim 20D_\perp$). The two requirements for an experimental data set to support a multiexponential model are (1) high time resolution to observe greater l components and (2) long-term observation to improve the signal-to-background ratio. The second requirement is an important characteristic of single-particle or single-molecule experiments where averaging is carried out in the time domain (cf. eq 30). These requirements may not always be attainable in an experiment. Therefore, it would be helpful to obtain analytical expressions under certain approximations to allow the determination of the dominating l components. This, in turn, will allow one to construct appropriate models that provide physical insights about the microscopic dynamics. For instance, if an analysis of experimental results indicates the dominating term belongs to an l component other than 2, then one has to consider models more complicated than a nearly spherical scatterer with cylindrical symmetry.

The next three sections illustrate how the general ideas discussed above are applied to different examples. One seeks to obtain analytical expressions using a perturbative approach for nearly spherical scatterers under the widely used annular illumination.

B. Rodlike Scatter Diffusers. The reduced linear dichroism for a single rodlike scatter-diffuser has been derived in eq 26. This expression is identical to the one obtained for single fluorescent molecule by Wei et al.;[24] therefore, their results are directly applicable. Generally, these authors found the rotational relaxation should exhibit multiexponential decay including $l = 2, 4, \ldots$ components with the $l = 2$ component being the dominant one. Furthermore, the weight of the $l = 2$ component increases from 0.84 for NA = 0 for the collimating objective to 0.99 for NA = 1.2.[23,24] These results can be understood graphically by plotting eq 26 in three dimensions, shown in Figure 4. In general, it is clear the shape of the reduced linear dichroism resembles an atomic d-orbital (e.g., $d_{x^2-y^2}$), described by the $l = 2$ spherical harmonics. It is therefore not surprising the decay is dominated by the $l = 2$ component. This graphical interpretation can be understood with the help of the connection formula,[29]

$$D^{(l)}_{m,0}(\Omega) = \sqrt{4\pi/(2l+1)}\, Y^*_{l,m}(\theta,\phi) \tag{37}$$

By virtue of the orthogonal property of the Wigner matrices in eq 33, the dominant l component in Green's function for rotational diffusion (eq 36) is selected out by the "shape" of the observable. If the shape of the observable resembles the $l = 2$ spherical harmonics function, the decay will be dominated by the $l = 2$ components. As the numerical aperture decreases, the deviation of eq 26 from a d-like orbital becomes more significant, hence the reduced weight in the $l = 2$ component.

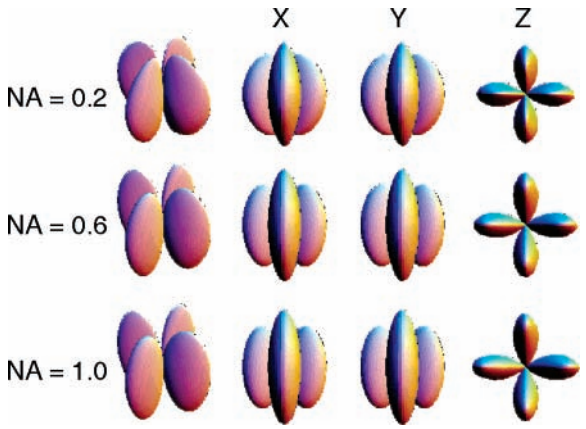

Figure 4. Three-dimensional shape for the reduced linear dichroism, χ_d (eq 26), for a single rodlike scatterer as observed through a collimating lens of numerical apertures (NA) 0.2, 0.6, and 1.0. The particle is assumed to be illuminated annularly with an NA = 1.2 dark-field condenser. The shape at NA = 1.0 resembles that of an atomic $d_{x^2-y^2}$ orbital but appears to deform along the Z direction (see the *X* and *Y* projections) as the NA of the collimating lens decreases. Columns 1 are viewed from (2, 1.3, 2.4), whereas columns 2−4 are viewed from $+X$, $+Y$, and $+Z$ directions, respectively.

C. Nearly Spherical Scatter Diffusers. For nearly spherical scatter-diffusers that exhibit cylindrical symmetry both in the diffusion and in the polarizability tensors, the reduced linear dichroism (eq 15) as calculated using eqs 28 and 29, can be expanded in powers of $(\alpha_{aniso}/\alpha_{iso})$. To the first-order approximation, this gives

$$\chi_d(t) \approx \frac{\alpha_{aniso}}{\alpha_{iso}} \frac{3C + CH}{4A + 3B + BH} \sqrt{\frac{8\pi}{15}} \left(Y_{2,2}(\theta,\phi) + Y_{2,-2}(\theta,\phi)\right)$$
$$= \frac{\alpha_{aniso}}{\alpha_{iso}} \frac{3C + CH}{4A + 3B + BH} \sqrt{\frac{2}{3}} \left(D^{(2)}_{-2,0}[\Omega_{LP}(t)] + D^{(2)}_{2,0}[\Omega_{LP}(t)]\right) \tag{38}$$

where the connection formula in eq 37 has been used to arrive at the second line. It is immediately clear that the signal vanishes for scatterers exhibiting isotropic scattering polarizability, or $\alpha_{aniso} \rightarrow 0$. This is true regardless of the shape or size of the particle. Furthermore, one would expect the decay of the correlation function to be dominated by the $l = 2$ components (cf. Figure 5). Experimental parameters such as NA of the collimating lens (affecting *A*, *B*, and *C*) and NA of the illumination optic (affecting *H*) only modifies the magnitude of the observable, χ_d, but not its three-dimensional shape. More specifically, for the reduced linear dichroism, one has

$$\langle \chi_d(t)\, \chi_d(0) \rangle = \frac{2}{15} \left(\frac{\alpha_{aniso}}{\alpha_{iso}}\right)^2 \left(\frac{3C + CH}{4A + 3B + BH}\right)^2 \left[\sum_{n=-2}^{2} (D^{(2)}_{n,0}(\Omega_{DP}))^2 \times e^{-6D_\perp t + n^2(D_{||} - D_\perp)t}\right] \tag{39}$$

The above equation reduces to a single-exponential decay when $(D_{||} - D_\perp) \rightarrow 0$. This procedure can be used to obtain higher-order terms in $(\alpha_{aniso}/\alpha_{iso})$ should the experimental data indicate an l dependence that is higher than $l = 2$. When the NA of the collimating lens approaches zero (experiment without high-NA collimating lens), the magnitude of this correlation function approaches $2/15 = 0.13$, i.e., $\lim_{\Delta \rightarrow 0}[(3C + CH)/(4A + 3B + BH)]^2 \rightarrow 1$. In general, just as the three-dimensional shape of the reduced linear dichroism depends on the NA of the collimating lens (cf. Figure 5), the magnitude of the correlation function depends on the NA for the incident illumination as well as on the NA for the collimating lens. The prefactor is

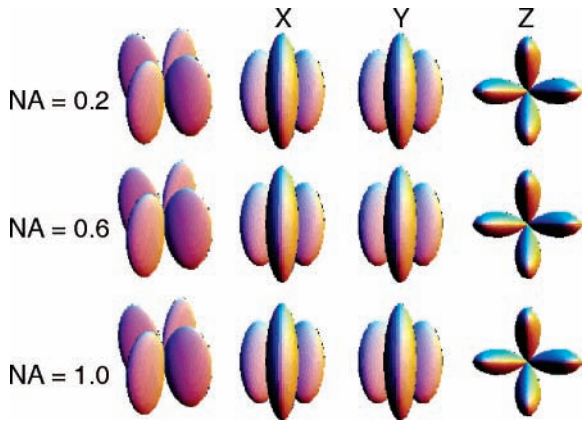

Figure 5. Three-dimensional shape for the reduced linear dichroism, χ_d (eq 38), for a nearly spherical scatterer as observed through a collimating lens of numerical apertures (NA) 0.2, 0.6, and 1.0. The particle is assumed to be illuminated annularly with an NA = 1.2 dark-field condenser. The shapes are seen to be independent of the NA of the collimating lens. Columns 1 are viewed from (2, 1.3, 2.4), whereas columns 2−4 are viewed from $+X$, $+Y$, and $+Z$ directions, respectively.

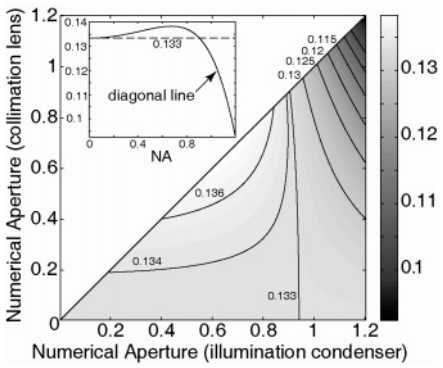

Figure 6. Amplitude of the time-correlation function in the fluctuation of reduced linear dichroism (eq 39) as a function of the numerical apertures for the collimation lens and illumination condenser. The inset displays the amplitude along the diagonal line as a function of the numerical aperture, with the dashed line indicating $2/150 \doteq 133$. A maximum is seen to occur when the numerical apertures for both the collimating and illuminating lenses are at ~0.675. The index of refraction for the medium is assumed to be 1.33 for these calculations.

plotted as a function of the numerical apertures and is displayed in Figure 6. Because all the setup-dependent coefficients are constant for a given experiment, eq 39 provides a way to directly measure the relative anisotropy of a particle ($\alpha_{aniso}/\alpha_{iso}$), as well as its distribution among an ensemble of particles.

Up to this point, the discussions have focused on the general aspects of the theoretical framework, in which the explicit form of the polarizability tensor, α, has not been specified. New experimental observations, on the other hand, combined with certain theoretical models are likely shed new light on the manner by which the various microscopic parameters—the polarizability tensor, the diffusion tensor, and the particle shape—are coupled together to give rise to the observations. The next section discusses one such example.

D. Spectral Fluctuations. As indicated in eq 1, the polarizability tensor is a function of the frequency of the incident light. Therefore, in addition to fluctuations in the polarizations of the scattered light as the particle undergoes rotational diffusion, one would expect to observe fluctuations in the scattering spectrum as well.[18] For this kind of experiment, a multichromatic or white light is used as an illumination source. To separate the intensity contributions due to polarization fluctuations from those due to spectral fluctuations, a spectral filter is placed *after* the polarization analyzer (cf. Figure 1). The spectral filter may reflect light with frequencies greater than its cutoff frequency (ω_0) to give the I_B signal, and transmit light with frequencies lower than ω_0 to give the I_R signal. Analogous to the reduced linear dichroism, the quantity of interest is the reduced spectral contrast, defined by

$$\chi_{Xs}(t) = \frac{I_{X,R}(t) - I_{X,B}(t)}{I_{X,R}(t) + I_{X,B}(t)} \quad \text{or} \quad \chi_{Ys}(t) = \frac{I_{Y,R}(t) - I_{Y,B}(t)}{I_{Y,R}(t) + I_{Y,B}(t)} \tag{40}$$

where the subscript indicates that the spectral contrast is measured after the X or Y polarization analyzer. Using the X-polarized scattering light as an example, the origin of the spectral fluctuation can be made more apparent by re-expressing eq 28 in terms of $\alpha_1(\omega)$ and $\alpha_3(\omega)$ to arrive at

$$I_{s,\circlearrowright,X} = W_{11}\alpha_1(\omega)^2 + W_{13}\alpha_1(\omega)\,\alpha_3(\omega) + W_{33}\alpha_3(\omega)^2 \tag{41}$$

where

$$W_{11} = \frac{1}{2}(A+B)(3+H) - \frac{1}{4}(A+4B+3AH+4BH)\sin^2\theta - (C+CH)\cos 2\phi \sin^2\theta + \frac{1}{4}(B+3BH)\sin^4\theta + \frac{1}{4}(C+3CH)\cos 2\phi \sin^4\theta \tag{42}$$

$$W_{13} = \frac{1}{2}(B+3BH)\sin^2\theta + \frac{1}{2}(C+3CH)\cos 2\phi \sin^2\theta - \frac{1}{2}(B+3BH)\sin^4\theta - \frac{1}{2}(C+3CH)\cos 2\phi \sin^4\theta \tag{43}$$

$$W_{33} = \frac{1}{2}(A-AH) + \frac{1}{4}(A+2B-2BH+3AH)\sin^2\theta + \frac{1}{2}(C-CH)\cos 2\phi \sin^2\theta + \frac{1}{4}(B+3BH)\sin^4\theta + \frac{1}{4}(C+3CH)\cos 2\phi \sin^4\theta \tag{44}$$

Therefore, as the particle rotates the θ and ϕ angles change. This in turn alters the magnitudes of W_{11}, W_{13}, and W_{33} such that the relative contributions from the $\alpha_1(\omega)^2$, $\alpha_1(\omega)\,\alpha_3(\omega)$, and $\alpha_3(\omega)^2$ terms will also change as a function of time. If the differences in the spectral densities of $\alpha_1(\omega)$ and $\alpha_3(\omega)$ are experimentally detectable, one is expected to observe spectral fluctuations that are correlated with the rotational dynamics. Using eq 41, the "red" and the "blue" components of the scattering spectrum can now be defined as

$$I_{X,R} = W_{11}\int_{\omega_0}^{\infty}\alpha_1(\omega)^2\,d\omega + W_{13}\int_{\omega_0}^{\infty}\alpha_1(\omega)\,\alpha_3(\omega)\,d\omega + W_{33}\int_{\omega_0}^{\infty}\alpha_3(\omega)^2\,d\omega$$

and

$$I_{X,B} = W_{11}\int_{-\infty}^{\omega_0}\alpha_1(\omega)^2\,d\omega + W_{13}\int_{-\infty}^{\omega_0}\alpha_1(\omega)\,\alpha_3(\omega)\,d\omega + W_{33}\int_{-\infty}^{\omega_0}\alpha_3(\omega)^2\,d\omega$$

respectively. In an experiment, the upper and lower bounds in the above expressions may be defined by the dichromatic filters used. The choice of the optical filter does not affect the results. The goal here then is to apply the theoretical framework to determine the dominant l-components in the time correlation function, $\langle\chi_{Xs}(t)\,\chi_{Xs}(0)\rangle$, and to relate such a theoretical understanding to experimental observations.

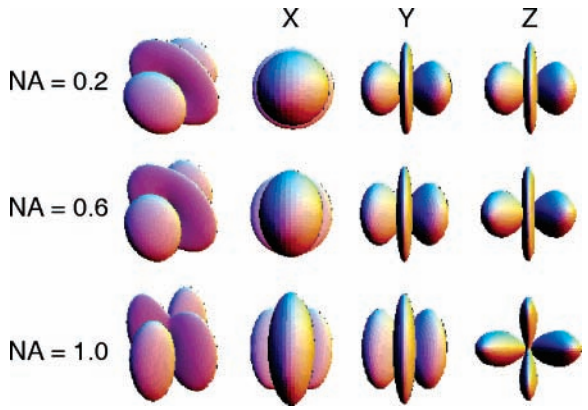

Figure 7. Three-dimensional shape for the reduced color contrast along X-polarized light, χ_{xs} (eq 47), for a nearly spherical scatterer as observed through a collimating lens of numerical aperture (NA) 0.2, 0.6, and 1.0. The particle is assumed to be illuminated annularly with an NA = 1.2 dark-field condenser. The three-dimensional shape can be seen to change significantly as the NA of the collimating lens changes. Yet, as eq 47 indicates, they all belong to the $l = 2$ spherical harmonics. Therefore, the overall rotational dynamics under this approximation still follows the $l = 2$ pattern. Columns 1 are viewed from (2, 1.3, 2.4), whereas columns 2−4 are viewed from the $+X$, $+Y$, and $+Z$ directions, respectively.

The problem at hand requires the use of a model for the polarizability tensor that explicitly incorporates the frequency response. For example, one may use the electrostatic approximation for spheroids (Rayleigh−Gans model):[15,41−43]

$$\alpha_i = \frac{4\pi}{3} a_1 a_2 a_3 \frac{\epsilon_r(\omega)}{1 + L_i \epsilon_r(\omega)} \tag{45}$$

where a_i is the semimajor (semiminor) axis along the ith polarizability principal component with $a_1 \leq a_2 \leq a_3$, $\epsilon_r(\omega) = \epsilon_m(\omega) - 1$ is the reduced relative permittivity, and L_i is the shape factor defined by

$$L_i = \frac{a_1 a_2 a_3}{2} \int_0^\infty \frac{dq}{(a_i^2 + q) f(q)} \tag{46}$$

with $f(q) = \sqrt{(q+a_1^2)(q+a_2^2)(q+a_3^2)}$. In accordance with the previous sections, here one focuses on cases that exhibit a cylindrical symmetry under annular illumination. This model has been shown to work reasonably well even with metallic nanorods (within linear scaling when compared with experiments).[44,45]

Equation 41 indicates that, in general, the correlation function, $\langle \delta\chi_{xs}(t)\, \chi_{xs}(0)\rangle$, will show complicated multiexponential behavior. However, for nearly spherical symmetric scatter-diffusers, analytical expressions can be obtained to afford physical insights. It can be shown that to the lowest order approximation in ξ, the angle-dependent part of the reduced spectral contrast—giving rise to spectral fluctuations as the particle undergoes rotational Brownian motion—has the following form

$$\delta\chi_{xs}(t) \propto \xi F_2(\omega_0,\epsilon_r)\left[-\frac{2A + 6AH + 6B + 2BH}{12A + 9B + 3BH} D^{(2)}_{0,0} + \sqrt{\frac{2}{3}} \frac{3C + CH}{4A + 3B + BH} (D^{(2)}_{2,0} + D^{(2)}_{-2,0})\right] \tag{47}$$

where $\xi \equiv a_{major}/a_{minor} - 1$ with a_{major} and a_{minor} being the semimajor and semiminor axes of the particle, respectively. A series of graphical representations for eq 47 as calculated using a collimating lens of different numerical aperture is displayed in Figure 7. Therefore, the spectral fluctuations at this level of approximation can be visualized as three-dimensional rotational diffusion of these objects. More specifically, the time correlation in the fluctuations of the reduced spectral contrast decays as $l = 2$, regardless of the shape of the particle (outlined in the Supporting Information):

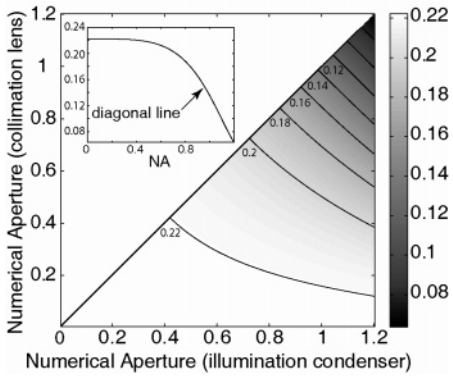

Figure 8. Numerical aperture-dependent amplitude of the time-correlation function in the fluctuation of reduced spectral contrast (eq 48) as a function of the numerical apertures for the collimation lens and illumination condenser. The inset displays the amplitude along the diagonal line as a function of the numerical aperture. The index of refraction for the medium is assumed to be 1.33.

$$\langle \delta\chi_{xs}(t)\, \delta\chi_{xs}(0)\rangle \approx \xi^2 F_2(\omega_0,\epsilon_r)^2 \times \left(\frac{6C^2(3+H)^2 + 4(A + 3AH + 3B + BH)^2}{45(4A + 3B + BH)^2}\right) \times \left[\sum_{n=-2}^{2} (D^{(2)}_{n,0}(\Omega_{DP}))^2 e^{-6D_\perp t + n^2(D_{||} - D_\perp)t}\right] \tag{48}$$

where $F_2(\omega_0,\epsilon_r)$, defined in the Supporting Information, is a function of the cutoff frequency of the reduced relative permittivity of the particle-medium system (ϵ_r) and the dichromatic mirror for discriminating the blue and the red portion of the scattering spectrum (ω_0). Analogous to the case in reduced linear dichroism, the magnitude of the correlation function depends on the deviation from a perfect sphere (ξ), the experimental configuration ($F_2(\omega_0,\epsilon_r)$ and the term contained in the parenthesis), and the relative orientation of the polarizability tensor and the diffusion tensor, Ω_{DP}. The formulation presented above also predicts that the spectral fluctuation vanishes for a perfect sphere, $\xi = 0$. Furthermore, although the model explicitly incorporates the particle size in the polarizability, the spectral fluctuation is independent of the particle size at this level of approximation. The experimental configuration-dependent prefactor is found to approach $2/9 = 0.22$ as the NA of the collimating lens approaches 0, independent of the NA of the illumination condenser. Figure 8 shows how the magnitude of the correlation depends on the NA of the illumination condenser as well as on the NA of the collimation lens. Because the prefactor is fixed for a given experiment, eq 48 in principle can be used to characterize the extent to which a particle deviate from being a perfect sphere, as well as the distribution of this parameter in an ensemble of particles.

5. Summary

A formal connection between the microscopic polarizability tensor of a light scattering nanoparticle (or nanostructure) and the far-field detected signal has been established. The use of this procedure was illustrated using two typical experimental

configurations, grazing-angle and dark-field annular illumination. The theoretical framework established here is general and is expected to contribute to the quantitative understanding of experimental results. Further insights for particles of more complicated geometries that are beyond dipole approximation can be obtained, for example, with the aid of such theoretical model as the discrete-dipole approximation,[46,47] which has been shown to be applicable to metallic nanostructures.[48] As a corollary, a method for using light scattering to rapidly imaging the absolute orientation of a nanostructure with a dominant polarizability tensorial component has also been given. In principle, this imaging method can be used to monitor time-dependent changes in the orientation of individual nanoparticles, in particular those that are nonfluorescent.

The analysis for particles that appear immobile on the experimental time scale has been extended to cases in which the time scales of the particle dynamics and the experimental measurements are comparable. These results form the theoretical basis for rotational single-particle dynamic light scattering that takes into account practical experimental issues such as the use of annular illumination and the high numerical aperture microscope objective for light collection. Using reduced linear dichroism as the observable, the time correlation function for a nearly spherical nanoparticle exhibiting cylindrical symmetry is shown to decay exponentially with a time constant of $\sim(6D_\perp)^{-1}$. As an application of the theory, the case of spectrally resolved dynamic light scattering is discussed. Using a simple electrostatic model explicitly relating the spectral response in the polarizability tensor to the shape of a nanoparticle, the theory suggests that the spectral fluctuations due to the rotational Brownian motion of the particle may become detectable in single-particle dynamic light scattering experiments.

Compared to a fixed-angle illumination setup, the annular illumination configuration removes the azimuthal-angle dependence for the magnitude of the induced dipole. The high numerical aperture for collecting the light scattered from a single particle mixes polarization components[30] that are not observable in the zero numerical aperture configuration in conventional ensemble-averaged experiments. The reduced linear dichroism (or the reduced spectral contrast as defined in this article) that is typically used in single-particle or single-molecule experiments further makes it challenging to extract information about the particle's rotational relaxation from the time correlation functions. All these have been shown to significantly impact the way in which experimental results are understood in microscopic terms. The formulations presented in this article take into account these considerations in single-particle light scattering experiments and will assist in a better understanding of nanoscale structures and the dynamics they exhibit.

Acknowledgment. This work is supported by the U.S. Department of Energy under contract No. DE-AC03-76SF00098 and the National Science Foundation (CHE-0349284). The author is grateful for the helpful discussions with H. Cang and for the critical reading and careful comments for this paper by C. S. Xu and D. Montiel.

Supporting Information Available: An approximate treatment of reduced spectral contrast for the cases of a prolate and an oblate scatterer. This material is available free of charge via the Internet at http://pubs.acs.org.

References and Notes

(1) van Dijk, M. A.; Tchebotareva, A. L.; Orrit, M.; Lippitz, M.; Berciaud, S.; Lasne, D.; Cognet, L.; Lounis, B. *Phys. Chem. Chem. Phys.* **2006**, *8*, 3486.

(2) Sfeir, M. Y.; Wang, F.; Huang, L. M.; Chuang, C. C.; Hone, J.; O'Brien, S. P.; Heinz, T. F.; Brus, L. E. *Science* **2004**, *306*, 1540.

(3) Yu, Z. H.; Brus, L. *J. Phys. Chem. B* **2001**, *105*, 1123.

(4) Wong, S. S.; Brus, L. E. *J. Phys. Chem. B* **2001**, *105*, 599.

(5) Kalkbrenner, T.; Hakanson, U.; Sandoghdar, V. *Nano Lett.* **2004**, *4*, 2309.

(6) Lindfors, K.; Kalkbrenner, T.; Stoller, P.; Sandoghdar, V. *Phys. Rev. Lett.* **2004**, *93*.

(7) Wang, H.; Wu, Y. P.; Lassiter, B.; Nehl, C. L.; Hafner, J. H.; Nordlander, P.; Halas, N. J. *Proc. Natl. Acad. Sci. U.S.A.* **2006**, *103*, 10856.

(8) Nehl, C. L.; Liao, H. W.; Hafner, J. H. *Nano Lett.* **2006**, *6*, 683.

(9) Sherry, L. J.; Chang, S. H.; Schatz, G. C.; Van Duyne, R. P.; Wiley, B. J.; Xia, Y. N. *Nano Lett.* **2005**, *5*, 2034.

(10) Schultz, S.; Smith, D. R.; Mock, J. J.; Schultz, D. A. *Proc. Natl. Acad. Sci. U.S.A.* **2000**, *97*, 996.

(11) Mock, J. J.; Barbic, M.; Smith, D. R.; Schultz, D. A.; Schultz, S. *J. Chem. Phys.* **2002**, *116*, 6755.

(12) Jin, R. C.; Cao, Y. W.; Mirkin, C. A.; Kelly, K. L.; Schatz, G. C.; Zheng, J. G. *Science* **2001**, *294*, 1901.

(13) Sherry, L. J.; Jin, R. C.; Mirkin, C. A.; Schatz, G. C.; Van Duyne, R. P. *Nano Lett.* **2006**, *6*, 2060.

(14) Xu, C. S.; Cang, H.; Montiel, D.; Yang, H. *J. Phys. Chem. C* **2007**, *111*, 32.

(15) Bohren, C. F.; Huffman, D. R. *Absorption and Scattering of Light by Small Particles*; Wiley-VCH: Mörlenbach, 2004.

(16) Mock, J. J.; Smith, D. R.; Schultz, S. *Nano Lett.* **2003**, *3*, 485.

(17) Sonnichsen, C.; Alivisatos, A. P. *Nano Lett.* **2005**, *5*, 301.

(18) Perez-Juste, J.; Pastoriza-Santos, I.; Liz-Marzan, L. M.; Mulvaney, P. *Coord. Chem. Rev.* **2005**, *249*, 1870.

(19) Berne, B. J.; Pecora, R. *Dynamic Light Scattering: With Applications to Chemistry, Biology, and Physics*; Dover Publications: New York, 2000.

(20) Bartko, A. P.; Dickson, R. M. *J. Phys. Chem. B* **1999**, *103*, 11237.

(21) Bartko, A. P.; Dickson, R. M. *J. Phys. Chem. B* **1999**, *103*, 3053.

(22) Fourkas, J. T. *Opt. Lett.* **2001**, *26*, 211.

(23) Hinze, G.; Diezemann, G.; Basche, T. *Phys. Rev. Lett.* **2004**, *93*, 203001.

(24) Wei, C. Y. J.; Kim, Y. H.; Darst, R. K.; Rossky, P. J.; Vanden Bout, D. A. *Phys. Rev. Lett.* **2005**, *95*, 173001.

(25) Sönnichsen, C.; Geier, S.; Hecker, N. E.; von Plessen, G.; Feldmann, J.; Ditlbacher, H.; Lamprecht, B.; Krenn, J. R.; Aussenegg, F. R.; Chan, V. Z. H.; Spatz, J. P.; Möller, M. *Appl. Phys. Lett.* **2000**, *77*, 2949.

(26) Eah, S. K.; Jaeger, H. M.; Scherer, N. F.; Wiederrecht, G. P.; Lin, X. M. *J. Phys. Chem. B* **2005**, *109*, 11858.

(27) Ignatovich, F. V.; Novotny, L. *Phys. Rev. Lett.* **2006**, *96*, 013901.

(28) Cang, H.; Wong, C. M.; Xu, C. S.; Rizvi, A. H.; Yang, H. *Appl. Phys. Lett.* **2006**, *88*, 223901.

(29) Rose, M. E. *Elementary Theory of Angular Momentum*; Dover: New York, 1995.

(30) Axelrod, D. *Biophys. J.* **1979**, *26*, 557.

(31) Sönnichsen, C.; Franzl, T.; Wilk, T.; von Plessen, G.; Feldmann, J.; Wilson, O.; Mulvaney, P. *Phys. Rev. Lett.* **2002**, *88*, 077402.

(32) Pinchuk, A.; Schatz, G. *Nanotechnology* **2005**, *16*, 2209.

(33) Watkins, L. P.; Yang, H. *J. Phys. Chem. B* **2005**, *109*, 617.

(34) Watkins, L. P.; Yang, H. *Biophys. J.* **2004**, *86*, 4015.

(35) Montiel, D.; Cang, H.; Yang, H. *J. Phys. Chem. B* **2006**, *110*, 19763.

(36) Oshida, I.; Suzuki, K.; Hiroshim. T; Matoba, K.; Kondo, Y. *Jpn. J. Appl. Phys.* **1968**, *7*, 561.

(37) Bar-Ziv, R.; Meller, A.; Tlusty, T.; Moses, E.; Stavans, J.; Safran, S. A. *Phys. Rev. Lett.* **1997**, *78*, 154.

(38) Debye, P. J. W. *Polar Molecules*; The Chemical Catalog Company Inc.: New York, 1929.

(39) Favro, L. D. *Phys. Rev.* **1960**, *119*, 53.

(40) Szabo, A. *J. Chem. Phys.* **1984**, *81*, 150.

(41) Gans, R. *Ann. Phys.-Berlin* **1912**, *37*, 881.

(42) Gans, R. *Ann. Phys.-Berlin* **1915**, *47*, 270.

(43) Papavassiliou, G. C. *Prog. Solid State Chem.* **1979**, *12*, 185.

(44) Link, S.; El-Sayed, M. A.; Mohamed, M. B. *J. Phys. Chem. B* **2005**, *109*, 10531.

(45) Link, S.; Mohamed, M. B.; El-Sayed, M. A. *J. Phys. Chem. B* **1999**, *103*, 3073.

(46) Purcell, E. M.; Pennypacker, C. R. *Astrophys. J.* **1973**, *186*, 705.

(47) Draine, B. T.; Flatau, P. J. User Guide for the Discrete Dipole Approximation Code DDSCAT 6.1 (http://arxov.org/abs/astro-ph/0409262v2), 2004.

(48) Kelly, K. L.; Coronado, E.; Zhao, L. L.; Schatz, G. C. *J. Phys. Chem. B* **2003**, *107*, 668.